Geometrical accuracy and fusion of multimodal vascular images: A phantom study

Nicolas Boussion
Laboratory of Biorheology and Medical Ultrasonics, Research Center, University of Montreal Hospital, Québec H2L 2W5, Canada

Gilles Soulez
Department of Radiology, University of Montreal Hospital, Québec H2L 2W5, Canada

Jacques A. De Guise
Laboratory of Imaging and Orthopedics, Research Center, University of Montreal Hospital, Québec H2L 2W5, Canada

Michel Daronat, Zhao Qin, and Guy Cloutier[a)]
Laboratory of Biorheology and Medical Ultrasonics, Research Center, University of Montreal Hospital, Québec H2L 2W5, Canada

(Received 10 December 2003; revised 11 March 2004; accepted for publication 30 March 2004; published 24 May 2004)

The aim of this work was to compare the geometrical accuracy of x-ray angiography, magnetic resonance imaging (MRI), x-ray computed tomography (XCT), and ultrasound imaging (B-mode and IVUS, or intravascular ultrasound) for measuring the lumen diameters of blood vessels. An image fusion method was also developed to improve these measurements. The images were acquired from a phantom that mimic vessels of known diameters. After acquisition, the multimodal images were coregistered by manual alignment of fiducial markers, and then by maximization of mutual information. The fusion method was performed by means of a fuzzy logic modeling approach followed by a combination process based on a possibilistic theory. The results showed (i) the better geometrical accuracy of XCT and IVUS compared to the other modalities, and (ii) the better accuracy and smaller variability of fused images compared to single modalities, with respect to most diameters investigated. For XCT, the error varied from 0.4% to 5.4%, depending on the vessel diameter that ranged from 0.93 to 6.24 mm. For IVUS, the error ranged from −0.3% to 1.7% but the smallest vessel (0.93 mm) could not be investigated because of the probe size. Compared to others fusion schemes, the XCT-MRI fused images provided the best results for both accuracy (from −1.6% to 0.2% for the three largest vessels) and robustness (mean relative error of 1.9%). To conclude, this work underlined both the usefulness of the multimodality vascular phantom as a validation tool and the utility of image fusion in the vascular context. [DOI: 10.1118/1.1751124]

Key words: vascular phantom, medical imaging, image fusion, geometrical accuracy, ultrasonography, magnetic resonance imaging, computerized tomography, x-ray angiography

I. INTRODUCTION

Several imaging modalities can be used clinically to investigate the severity of vascular pathologies such as aneurysms,[1] stenoses,[2] and malformations.[3] Functional and morphologic imaging techniques provide data that can be complementary, but a single modality alone may lead to a difficult decision about a potential abnormality.[4] Actually, the physical process at the origin of each modality leads to specific advantages but also to individual limitations.[5–7] The partial volume effects, limited spatial resolution, artifacts, and signal-to-noise ratios are modality-dependent parameters that must be taken into account when investigating a given pathology. In a day-to-day clinical practice, a compromise must be reached between the diagnostic value of each imaging technique, patient security, and comfort (length of acquisition, invasiveness, radiation, etc.). Furthermore, in some situations of presurgical exploration, it may be impossible to perform an optimal set of examinations. For example, deterioration of an image induced by vascular calcifications can be a major limitation in Doppler and B-mode ultrasound or computed tomography angiography whereas a metallic stent induces more deterioration on images obtained with magnetic resonance angiography.

In this clinical context of vascular investigation, the aim of the study was first to assess the accuracy of various modalities for the measurement of lumen diameters. From the postulate that x-ray computed tomography (XCT) may provide the best spatial resolution,[8] the purpose was to compare the three-dimensional (3D) geometric accuracy of XCT, digital subtraction angiography (DSA), magnetic resonance imaging (MRI), and ultrasound (US) imaging (B-mode and intravascular or IVUS). To our knowledge, the comparison of multimodal imaging obtained from a single realistic vascular phantom has never been addressed, and this was made possible by the development of a multimodality phantom with fiducial markers visible in DSA, XCT, MRI, and US.[9] Fur-

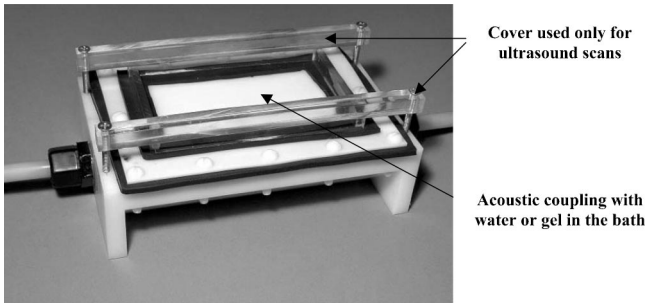

FIG. 1. External view of the multimodality vascular flow phantom used. The cover for ultrasound scans and metallic screws maintaining it were removed for MRI and x-ray based acquisitions.

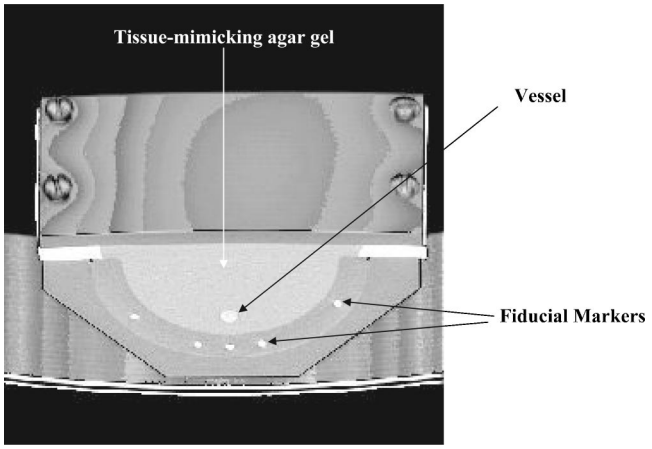

FIG. 2. Reconstructed 3D view of the phantom from an x-ray computed tomography scan. The phantom is cut transversally to show the vessel and five fiducial markers (five of the 25 markers included in the phantom are visible on this view).

thermore, this framework of multimodality suggested to investigate image fusion. Actually, the fusion approach recently demonstrated high robustness in various medical fields such as the planning of epilepsy surgery,[10] heart disease risk assessment,[11] or ultrasound image segmentation.[12] Frequently, scans from different modalities are available to the clinician for confirming a diagnosis. Thus the second objective of this study was to build a multimodal image combination method hopefully able to offer a better evaluation than single modalities. More specifically, the goal was to verify the hypothesis that image fusion from two different modalities can improve the diagnosis of vascular diseases by enhancing 3D geometric measurements of vessel lumen sizes.

II. METHODS

A. Phantom and modeled vessels

To obtain reliable gold standard measurements, images of a multimodality phantom were acquired. The method for fabricating the phantom (Fig. 1) is described elsewhere.[9] It consisted of a semispherical container filled with a tissue-mimicking material (agar-based solidified gel) in the middle of which was embedded a vessel connected to an inlet and an outlet.

The vessel was made by a lost-material casting technique, the interface between the lumen and agar was a thin impermeable layer of latex, so as to avoid possible diffusion of water or contrast agent towards the agar gel. To facilitate the spatial alignment of images, 25 fiducial markers were embedded in the structure of the phantom (in a semicylindrical layer of agar-oil mixture gel surrounding the vessel). They consisted of five parallel and asymmetrical rows of five glass spheres. Glass was chosen because it provides good contrast with agar-based gel in x-ray and US modalities. The use of a paraffin oil in the bottom layer of the agar-based gel allowed the glass balls to be visible in hyposignal with MRI. The diameter of the spheres was 3 mm (Fig. 2). These markers were not visible in IVUS because of the small field of view of this modality when using a 20 MHz probe.

The vessel had a multistep geometry: it was made up of four adjacent pieces, each of 20 mm long. The diameter of these four contiguous segments was, respectively, 4.16, 2.34, 0.93, and 6.24 mm. A precise numerical version of the vessel and fiducial markers was computed as a 3D matrix of $0.1 \times 0.1 \times 0.1$ mm^3 voxels (Fig. 3). The aim was to help with aligning the images and facilitating their spatial coregistration. The slices of this numerical phantom were designed perpendicularly to the axis of the vessel segments.

B. Image acquisition

Five different scans of the phantom were obtained, all with standard clinical devices. The vessel was filled with water and contrast agent when necessary, and then set to 100 mmHg (equivalent to the physiological human blood pressure). In all scans, the concentration of the x-ray and MRI contrast agents was carefully selected to mimic the image intensity enhancement obtained on clinical radiological images under normal physiological flowing conditions. As reported earlier,[9] pressurizing the vessel to 100 mmHg allowed one to obtain a precision of 0.004 mm when a comparison is made between the diameter of the lumen and that of the template used to produce it. Contrast agents were a 430 mg/ml radiopaque contrast medium (Conray 43, Mallinckrodt Medical Incorporated, Pointe-Claire, Québec, Canada)

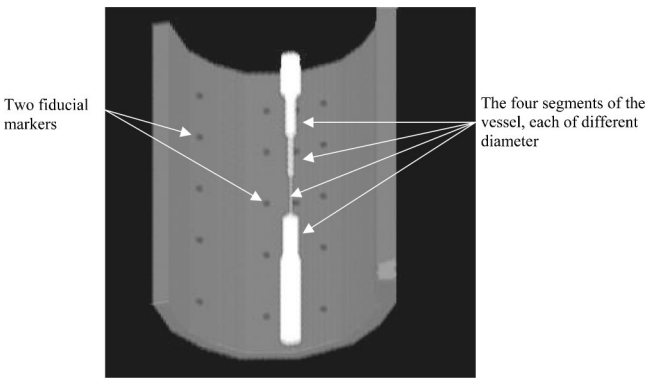

FIG. 3. 3D view of the numerical version of the phantom's main parts: vessel and markers.

for DSA, a 2.8% solution of 430 mg/ml iothalamate meglumine (Conray 43) diluted in a 0.9% NaCl solution for XCT, and a 1.8 mmol/l of Magnevist contrast agent (Berlex Canada Incorporated, Lachine, Québec, Canada) diluted in 0.9% NaCl solution for MRI.

The MR angiography was performed with a Magnetom Vision machine 1.5 T (Siemens, Erlangen, Germany). Images were set in a 300×512 field of view and reconstructed as a matrix of $0.98\times0.76\times0.84$ mm^3 voxels. XCT was performed with a Picker 5000 scanner (Picker International, Cleveland Heights, OH), using a slice thickness of 1 mm, with a pitch of 1.25 mm and a reconstruction interval of 1 mm. IVUS images were acquired under fluoroscopy guidance with an In-Vision Gold ultrasound system (Jomed, Lilestraten, The Netherlands) equipped with a 20-MHz probe inserted in the vessel lumen via a catheter guide. A motorized ''pull-back'' technique was used to reconstruct the 3D geometry (eight slices per millimeter). This latter method consisted of pulling the IVUS catheter at a constant speed within the vessel and, concurrently, acquiring images at constant time intervals. X-ray planar angiography was undertaken during the same session. A single acquisition was done in anterior-posterior, 30° left anterior oblique and right anterior oblique projections (field of view 17 cm, tube-intensifier distance 82 cm, table height 105 cm, matrix size 512×512, 25 kV, 60 mA) on a HICOR/ACOM-TOP device (Siemens, Erlangen, Germany).

B-mode US images were acquired with a Logiq9 device (General Electrics Medical Systems, Waukesha, WI), the 6 MHz phase-array transducer (probe number 7L) being automatically translated linearly above the phantom by a motorized axis (3.25 slices by millimeter), perpendicularly to the vessel (dynamic range 90 dB, no edge enhancement, no frame average). For both B-mode and IVUS US scans, the transducer selection frequency was made in the context of lower limb vascular evaluations.

All multimodality images were either archived on the PACS system of the hospital or directly recorded on CDs and then directed to a PC hard drive where further processing was performed.

C. Spatial coregistration

Spatial reconstruction of the images was a mandatory prerequisite step before performing measurements and fusion. Each image was separately coregistered with the numerical 3D phantom for reconstruction with isotropic voxels. The process was performed by means of a manual prealignment followed by accurate fully automated coregistration. The first step consisted of manual alignment of the images with the numerical virtual phantom, using the ImageJ software (Wayne Rasband, Research Services Branch, National Institute of Mental Health, Bethesda, MD). This was performed with the help of the fiducial markers, except for IVUS where the interface between the segments of different diameter were used as landmarks. The quality of this step was assessed visually, by superimposing as precisely as possible the center of the fiducial markers of both numerical and real phantoms. The images were then precisely registered to the numerical vessel by maximization of mutual information,[13,14] a robust similarity measure. The reconstructed voxels had a dimension of $0.1\times0.1\times0.1$ mm^3. Thus, at the end of this step, all images were reformated identically and represented in the same geometric space, allowing reliable comparisons of the geometric measures.

Thanks to this two step coregistration, based on the markers and a well-known algorithm, the images were superposed as much precise as possible. However, even if they were not, the fuzzy modeling process that is presented later would correct it by constructing fuzzy contours that allow the spatial uncertainty to be managed.

D. Size of the lumen

1. Diameter measurements

The inner diameter of the vessel sections was measured after segmentation. The same method was used for each modality (excluding DSA): the segmented contour was the interface between the lumen and the inner side of the vessel. It was determined at the maximum of the gradient norm. This latter expresses the local difference between pixel values and is defined, in the discontinuous case, by

$$|\nabla A[i,j]| = \sqrt{A_j^2[i,j]+A_i^2[i,j]},$$

with

$$A_i[i,j]=A[i+1,j]-A[i,j],$$

$$A_j[i,j]=A[i,j+1]-A[i,j],$$

and $A[i,j]$=value of pixel (i,j).

After segmentation, the barycenter B of the segmented contour in each slice was ascertained. The distance between B and every point of the boundary was then calculated and multiplied by 2 to obtain the diameter value. The mean (M) and standard deviation (SD) of the diameters were evaluated from 20 slices selected within each of the four segments of the vessel with different sizes. For DSA, the planar acquisition mode prevented us from measuring diameters with this method. Here, diameters were evaluated manually by using a caliper, after calibration of the pixel size thanks to the known distance between fiducial markers.

2. Statistical data analysis

The global robustness of the various methods (single modalities and fused images) with respect to all diameters was investigated by calculating the mean relative error (MRE) of each technique compared to the gold standard (actual diameter of the vessels). For each modality and for each fused image, MRE was estimated by calculating the mean relative error of all measures of all segments. The limits and the length of the confidence interval (CI) of MRE were computed to help assess the accuracy of the different modalities and combined images. The limits of CI were calculated as follows:

$$CI_{inf} = m_{MRE} - T\sqrt{\frac{SD_{MRE}}{N-1}},$$

$$CI_{sup} = m_{MRE} + T\sqrt{\frac{SD_{MRE}}{N-1}},$$

where m_{MRE} and SD_{MRE} are, respectively, the mean and the standard deviation of MRE, N is the total number of measures, and T is the critical two-tailed t value for $N-1$ degrees of freedom.[15] The length of CI was defined as $CI_{sup} - CI_{inf}$, where the subscripts sup and inf indicate the superior and inferior limits of the confidence interval.

E. Fusion process

1. Common modeling

Five fusion strategies were tested: XCT-MRI, MRI-IVUS, MRI-B-mode, XCT-IVUS, and XCT-B-mode. They were selected by considering potential clinical investigations on a given patient. In each case, the two modalities to be fused greatly differed in terms of content, even if they provided pieces of information about the same object. Thus the first step of the process consisted of translating the initial images into a common mathematical framework, which was chosen as the fuzzy set theory.[16] The main value of this theory lies in the management of imprecision intrinsic to medical images, due to the finite spatial resolution or the partial volume effect, as already stated. The theory of fuzzy sets replaces the two-valued set membership function (0 or 1) of crisp sets theory with a real-valued function, which leads to define membership to a fuzzy set as a degree of truthfulness or possibility. One assigns a real value $F(x)\,[0 \leqslant F(x) \leqslant 1]$ to assertions as an indication of their degree of reliability. By using this notion, the fuzzyfication of the acquired images was performed as follows.

As a first step, the lumen contour of the images was segmented by calculating the maximum gradient as explained earlier. This boundary was then fuzzyfied by means of a 3D distance map (chamfer method[17]), providing the distance between the said contour and each point of the volumetric image. The mean diameter (D) of the segmented contour was then calculated and multiplied by 2.5%. This last value, referred to as the ''low threshold,'' served to build a margin of security around the segmented contour. Actually, the fuzzy contour F was defined as the set of voxels whose distance to the segmented boundary was ''less than $0.025 \times D$.'' Precisely, the voxels less distant than $0.025 \times D$ were considered as totally included into F (membership=1), while voxels more distant than $0.175 \times D$ from the segmented boundary (referred to as the ''high threshold'') were considered as totally excluded from the fuzzy set F (membership=0). For distances between $0.025 \times D$ and $0.175 \times D$, the membership value of the voxels linearly decreased from 1 to 0 (see Fig. 4 for a graphic description of the fuzzy contour membership function). The justification for the selection of the low and high thresholds is investigated later in this section.

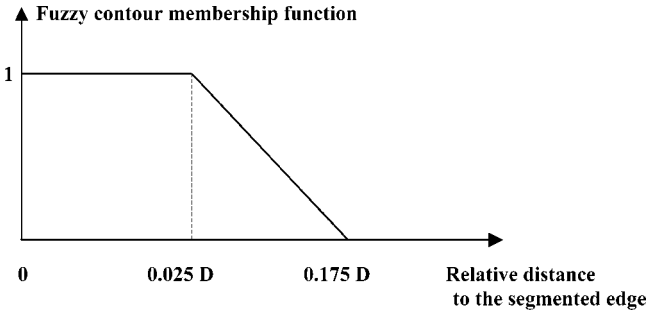

FIG. 4. Membership function to the fuzzy boundary F. D is a preliminary estimation of the vessel diameter.

Thus the resulting fuzzy image contained voxels more or less intense, according to their proximity to the segmented vessel edge (Fig. 5).

2. Fusion of the fuzzyfied images

a. Possibility theory: basic definitions. The main benefit of the possibilistic approach[18] is the ability to manage both uncertainty and imprecision with powerful fusion operators. The definitions below introduce the methods used in the current study.

If one considers a finite universe of discourse X and $P(X)$, the set of subsets of said universe, a possibility measure can be defined as a mapping $\Pi: P(X) \rightarrow [0,1]$ such that:

(i)

$$\Pi(\varnothing) = 0, \quad \Pi(X) = 1,$$

(ii)

$$\forall A \in X, \quad \forall B \in X, \quad \Pi(A \cup B) = \max[\Pi(A), \Pi(B)],$$

where $\Pi(A)$ expresses the possibility degree that the set A occurs. If $\Pi(A) = 0$, A is impossible and cannot occur, whereas if $\Pi(A) = 1$, A is totally possible (thus nothing can prevent A from occurring, but A *may not* occur). The possibility degrees can be defined more naturally by considering single elements of X instead of subsets. A *distribution of possibility* assigns values from $[0,1]$ to each element of X according to his possible membership to the subset A. A possibility distribution is a mapping π: $X \rightarrow [0,1]$ that must satisfy:

$$\max_{x \in X} \pi(x) = 1 \quad \text{(normalization condition)}.$$

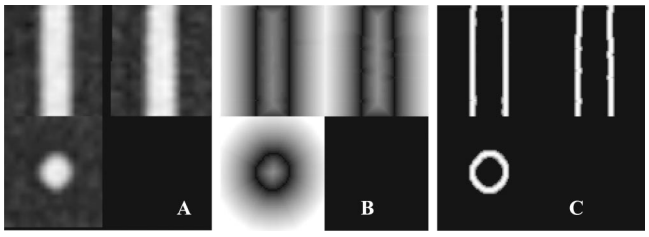

FIG. 5. Modeling process: the example of MRI. A: MRI sagittal, coronal, and transversal views of the 6.24-mm-diameter vessel. B: distance map (chamfer method) built from the presegmented contour of the vessel. C: final fuzzy contour.

A simple form of possibility distribution on X is the fuzzy membership function of a subset $A \subset X$, provided that it satisfies the normalization condition.

b. Fusion operator. Voxels in fuzzy maps have values in the continuous set [0,1], which allowed the use of fusion operators from the possibilistic theory in order to merge those maps.[19,20] The combination procedure from the possibilistic theory is dependent on the behavior of the operators. If x and y are two real numbers from [0,1], and F a fusion operator that aims to combine x and y, then F is:

(i) conjunctive if $F(x,y) \leqslant \min(x,y)$, which corresponds to a severe behavior;
(ii) disjunctive if $F(x,y) \geqslant \max(x,y)$, which corresponds to an indulgent behavior; and
(iii) cautious if $x \leqslant F(x,y) \leqslant y$, if $x \leqslant y$, or if $y \leqslant F(x,y) \leqslant x$ if $y \leqslant x$, which corresponds to a compromise behavior.

To simplify, F is cautious if $\min(x,y) \leqslant F(x,y) \leqslant \max(x,y)$, in such a way that min and max are often used to classify operators as conjonctive, disjunctive, or cautious. With such definitions, it is easy to demonstrate that any triangular-norm (t-norm) is a conjunctive operator, while any triangular-conorm (t-conorm) has a disjunctive behavior.[20] The probabilistic t-norm defined by $F(x,y) = x \times y$ was chosen to fuse our images because it is very simple and also conjunctive.[19] This latter property is well adapted here because a precise segmentation of the vessel was required and the fuzziness of the images had to be reduced to reinforce the reliability of the final segmentation. Other operators with severe behavior like the Zadeh t-norm [other name of $\min(x,y)$] and the Lukaziewicz t-norm $[\max(x+y-1,0)]$[19,21] were also tested but they gave results comparable to the probabilistic t-norm which was selected for its simplicity.

c. Management of reliability. In the case of conflict between images (different location of the vessel contours), the fusion process is able to manage the imprecision thanks to the operator presented in the previous section. However, according to the literature, XCT should provide the best geometrical accuracy because of its good spatial resolution.[8] Furthermore, IVUS imaging is also expected to be more accurate than MRI due to its high spatial resolution,[22] especially if one uses a high frequency ultrasound transducer. These considerations were taken into account in the fusion process by means of a weighted data aggregation procedure. The elegant linear approach proposed by Cron and Dubuisson,[23] defining a weighted combination rule, was chosen because it does not depend upon the operator. Basically, a weight ω_i is attached to each source i to fuse in such a way that the result of the fusion becomes:

$$F_{\omega 1,\omega 2}(x_1,x_2) = P(\omega_1,\omega_2) \times F(x_1,x_2) + x_1 \times P1(\omega_1,\omega_2) + x_2 \times P2(\omega_1,\omega_2),$$

$$\text{with } P1(\omega_1,\omega_2) = \begin{cases} 0 & \text{if } \omega_1 \leqslant \omega_2 \\ \dfrac{\omega_1 - \omega_2}{\omega_1} & \text{else,} \end{cases}$$

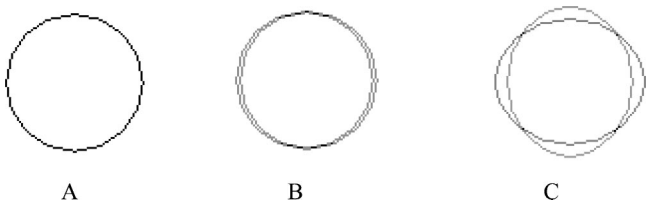

FIG. 6. Test images for studying the effect of the thresholds in the fuzzy membership construction, and for the evaluation of the weighting process. (A): two identical circles perfectly superimposed, (B): two identical circles horizontally shifted, and (C): two centered ellipses.

$$P2(\omega_1,\omega_2) = \begin{cases} 0 & \text{if } \omega_2 \leqslant \omega_1 \\ \dfrac{\omega_2 - \omega_1}{\omega_2} & \text{else,} \end{cases}$$

$$\text{and } P(\omega_1,\omega_2) = \begin{cases} 1 & \text{if } \omega_1 = \omega_2 = 0 \\ \dfrac{\min(\omega_1,\omega_2)}{\max(\omega_1,\omega_2)} & \text{else.} \end{cases}$$

As weights, $P(\omega_1,\omega_2)$, $P1(\omega_1,\omega_2)$, and $P2(\omega_1,\omega_2)$ belong to the real closed interval [0,1], and their sum is 1 because $F_{\omega 1,\omega 2}(x_1,x_2)$ represents a weighted sum.

Thus if $\omega_1 = \omega_2 = 0$, we have $P1(0,0) = P2(0,0) = 0$, and $P(0,0) = 1$, which leads to the cancellation of the weighting process: $F_{0,0}(x_1,x_2) = F(x_1,x_2)$. Actually, the weighting process will be cancelled as soon as the weights are equal $(\omega_1 = \omega_2)$. On the other hand, if $\omega_1 = 0.6$ and $\omega_2 = 0.4$, for instance, one obtains $P1(0.6,0.4) = 1/3$, $P2(0.6,0.4) = 0$, $P(0.6,0.4) = 2/3$, and $F_{0.6,0.4}(x_1,x_2) = 2/3F(x_1,x_2) + 1/3x_1$ in such a way that the knowledge provided by image 1 is partially added in the final fused image. This classical weighting method is a linear combination of the fused image with the initial image having the highest weight.[10]

The XCT, IVUS, MRI, and B-mode relative weight factors were selected to 1, 0.95, 0.8, and 0.7, respectively. These values were chosen by taking into account the geometrical accuracy of each modality according to the literature, and after visual assessment of the quality of the images collected from the vascular phantom.

3. Defuzzification

The resulting fused images remained fuzzy due to the closure property of the t-norms. A defuzzification was thus mandatory to provide the final object representing the real contour. This objective was achieved by extracting the skeleton of the fuzzy map with mathematical morphology tools.[24,25]

F. Impact of the low and high thresholds, role of the weighting process

As mentioned earlier, the construction of fuzzy contours was realized with a classical linear membership function, characterized by two thresholds already referred to as the ''low'' and ''high'' thresholds. The effect of the latter on the fusion process was evaluated by using two pairs of test images. The images of each generated couple were converted into fuzzy maps as described above, but with different low

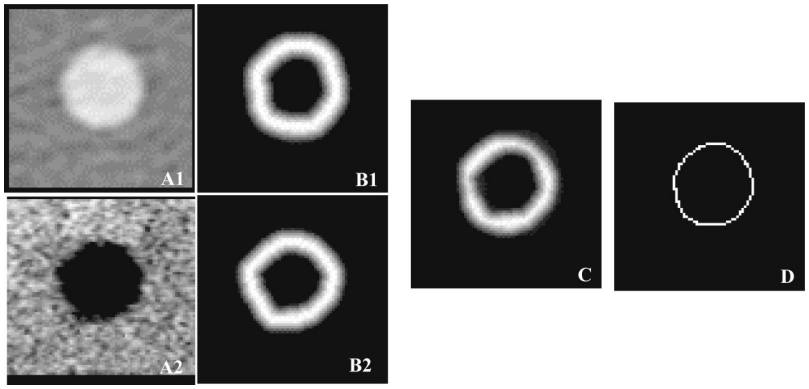

FIG. 7. Example of the XCT-B-mode US fusion process. A1, A2: XCT and B-mode US transversal views. B1, B2: fuzzy boundaries deduced from the presegmented lumen contour of A1 and A2. The real lumen–vessel interface is supposed to be included in each of these images. C: weighted fusion of B1 and B2 with the probabilistic *t*-norm. The width of this fused fuzzy contour is smaller than B1 and B2 due to the conjunctive property of the fusion operator. D: skeleton of the fuzzy map C, considered as the actual lumen–vessel interface. Transversal slices are shown for clarity but the whole process is 3D.

and high threshold values. The low threshold was changed from 0.025 to 0.175, while the high threshold ranged from 0.05 to 0.2. Then, the diameter of the fused image for each configuration and for each pair of test images was calculated. The test images were two identical circles perfectly superposed [diameter of 60 pixels, Fig. 6(A)], and two identical circles (diameter of 60 pixels) horizontally distant by two pixels [Fig. 6(B)]. The diameter of the fused images were compared to the actual size of the initial images.

A similar study was done to better understand the behavior of the weighting part of the fusion process. The ellipses presented in Fig. 6(C) were fused with weights ranging from 0.1 up to 0.9 for one ellipse and from 0.9 down to 0.1 for the other, both with steps of 0.1. These two centered ellipses were of dimension 56 pixels×64 pixels, and 64 pixels×56 pixels, and the mean and standard deviation of the diameter of their fusion also were evaluated.

III. RESULTS

A. Diameter measurements

1. Values obtained for the different diameters according to the methods

Figure 7 illustrates the modeling and combination processes through the example of XCT-B-mode US fusion. The main results of the present study are summarized in Table I. It shows the diameters of the vessel segments measured from single coregistered images and from bimodal fused images. The gold standard measures of the phantom also are presented to classify the studied modalities according to their geometric accuracy. The relative error, in percent, between the image diameters and the gold standard diameters are presented too. Some values are missing from Table I due to technical difficulties that are detailed in the Discussion.

TABLE I. Measured inner diameter. Absolute values (mean ± standard deviation) are given in millimeters and relative errors are shown in parentheses.

Gold standard	6.24	4.16	2.34	0.93
Angiography (calibrated)	5.88±0.15 (−5.8%)	3.99±0.15 (−4.1%)	2.20±0.12 (−6.0%)	0.86±0.18 (−7.5%)
XCT	6.16±0.10 (−1.3%)	4.23±0.09 (+1.7%)	2.35±0.12 (+0.4%)	0.98±0.08 (+5.4%)
MRI	6.17±0.13 (−1.1%)	4.19±0.15 (+0.7%)	2.42±0.10 (+3.4%)	1.56±0.12 (+67.7%)
B-mode US	6.30±0.21 (+1.0%)	4.26±0.27 (+2.4%)	2.43±0.23 (+3.8%)	[a]
IVUS	6.22±0.10 (−0.3%)	4.20±0.10 (+1.0%)	2.38±0.09 (+1.7%)	[b]
Fused XCT-MRI	6.14±0.08 (−1.6%)	4.17±0.06 (+0.2%)	2.36±0.08 (+0.9%)	1.05±0.08 (+12.9%)
Fused MRI-IVUS	6.21±0.05 (−0.5%)	4.21±0.09 (+1.2%)	2.39±0.05 (+2.1%)	
Fused MRI-B-mode	6.18±0.10 (−1.0%)	4.19±0.11 (+0.7%)	2.40±0.10 (+2.6%)	
Fused XCT-B-mode	6.20±0.08 (−0.6%)	4.17±0.10 (+0.2%)	2.33±0.10 (−0.4%)	
Fused XCT-IVUS	6.22±0.05 (−0.3%)	4.21±0.09 (+1.2%)	2.37±0.08 (−1.3%)	

[a]Vessel too small to be observed.
[b]IVUS probe too large (diameter 1.2 mm) to investigate the vessel.

TABLE II. Mean relative error and its confidence interval. Mean relative error values were calculated from the three largest vessels since data were not available in all modalities for the 0.93 mm diameter vessel.

Image	Mean relative error (%)	Confidence interval (%)	Length of the confidence interval (%)
Angiography	5.39	4.87–5.90	1.03
XCT	2.62	2.23–3.01	0.78
MRI	3.24	2.85–3.64	0.79
B-mode US	6.12	5.59–6.64	1.05
IVUS	2.44	2.10–2.78	0.68
Fused XCT-MRI	1.92	1.62–2.22	0.60
Fused MRI-IVUS	1.78	1.47–2.09	0.62
Fused MRI-B-mode	2.66	2.29–3.03	0.74
Fused XCT-B-mode	2.29	1.93–2.65	0.72
Fused XCT-IVUS	2.04	1.70–2.38	0.68

The first point that arises from Table I is the overall good accuracy provided by the various modalities. Except for the 0.93-mm-diameter vessel investigated by MRI, the relative error never exceeded 7.5% (maximum relative error for planar angiography). Concerning the largest vessel (6.24-mm-diameter), IVUS provided the most accurate estimation (relative error of −0.3%) but the other modalities gave satisfactory results as well. IVUS also gave good results for the other vessel diameters. XCT provided a good measurement of the smallest vessel (+5.4%), while MRI greatly overestimated it, probably because of partial volume effect (relative error of +67.7%). It is worth noticing the reduction in measurement quality for MRI when the diameters decreased. MRI also overestimated the 2.34 mm diameter (+3.4%), while XCT estimated it with high precision (+0.4%). B-mode US overestimated all diameters but overall the accuracy remained acceptable (maximal relative error of +3.8%). Lastly, planar angiography provided less accurate results and tended to underestimate the actual diameter values.

The fused images always provided good estimates of the actual diameters, even if some results were less accurate than single modalities. For example, the fusion of XCT and MRI gave lower precision than either XCT or MRI alone in three cases, but at the same time, the variability of the measures was improved as shown by the decrease of the standard deviations. Furthermore, the XCT-MRI fusion process failed (relative error 12.9%) for the 0.93-mm-diameter vessel, but it is not surprising since the latter was significantly overestimated by MRI. In this case, the fusion approach was thus not pertinent.

2. Global mean relative error (MRE)

Table II contains the value of MRE for each modality and for each fused image. It was calculated only from the diameters of the three largest vessels, since some experimental data were not available for the 0.93 mm diameter vessel.

This table shows that IVUS and XCT were the modalities with the lowest MRE (2.44% and 2.62%, respectively) and the shortest confidence interval (CI). This means that globally, these techniques better evaluated the three largest vessels compared to the other modalities, IVUS providing the best results.

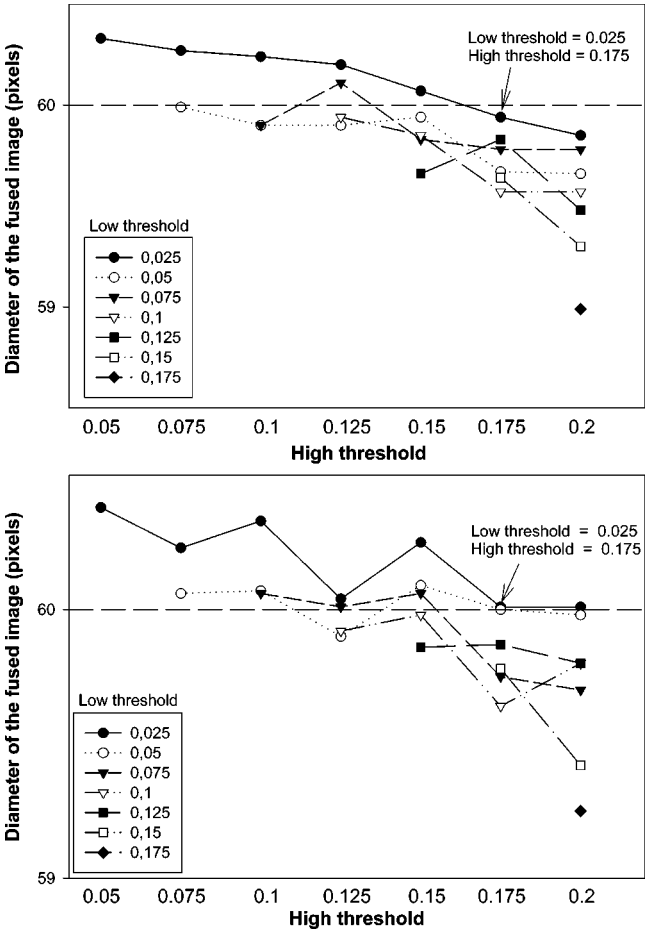

FIG. 8. Effect of the threshold selections on the measured diameter of the test images. Up: identical circles. Down: shifted circles.

Concerning fusion, MRE was lower for all fused images than IVUS or any other single modalities, except for MRI-B-mode fusion (MRE of 2.66% compared to 2.44% for IVUS and 2.62% for XCT). The confidence intervals are in agreement with this statement, the longest CI value being 0.74% for MRI-B-mode fusion (the values for single modalities ranged from 0.68% to 1.05%). The lowest errors were provided by MRI-IVUS and XCT-MRI fusions, while MRI-B-mode combination gave a relatively high MRE due to the higher variability in diameter measurements (see standard error values in Table I).

B. Influence of the thresholds and weights used in the fusion process

Figure 8 shows the impact of the low and high thresholds used to create the fuzzy contours on the estimate of the diameters of the fused test images. Both the low and high threshold values were varied between 0.025 and 0.175. As described earlier, shifted and identical circles with a diameter of 60 pixels were tested in order to investigate also the robustness of the threshold values with respect to a possible

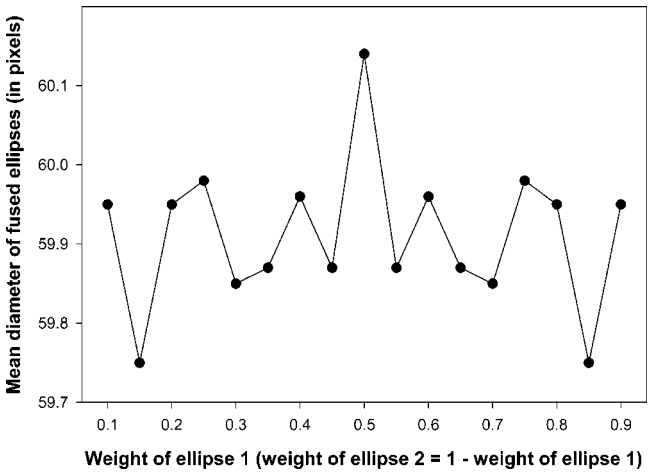

FIG. 9. Diameter of the fused ellipses according to the relative weights attributed to each of them.

inaccurate spatial registration. This figure first shows that these thresholds had a relatively low impact on the fusion process. This observation typically is an illustration of the flexibility of the fuzzy modeling that deals well with imprecision. Figure 8 also certifies that the selected low threshold of 0.025 and the high threshold of 0.175 provided a good estimation of the actual diameter in both cases. Comparable conclusions were also obtained with other tested diameters (results not shown), and this is why this set of thresholds was chosen for our modeling process.

Besides, the mean and standard deviation of the diameter of the fused ellipses [Fig. 6(C)] are, respectively, reported in Figs. 9 and 10. Let us recall that the aim was to assess the role of the weights in the fusion step. The maximum diameter was observed for identical weights (Fig. 9), i.e., when no specific weighting was applied ($\omega_1 = \omega_2 = 0.5$). In this configuration, the fused image was rather circular thus the standard deviation of the diameter was lower than in all other configurations (Fig. 10). Actually, when ω_1 and ω_2 differed, this standard deviation increased because the fused image tended to become an ellipse (ellipse 1 or ellipse 2 according to the weights).

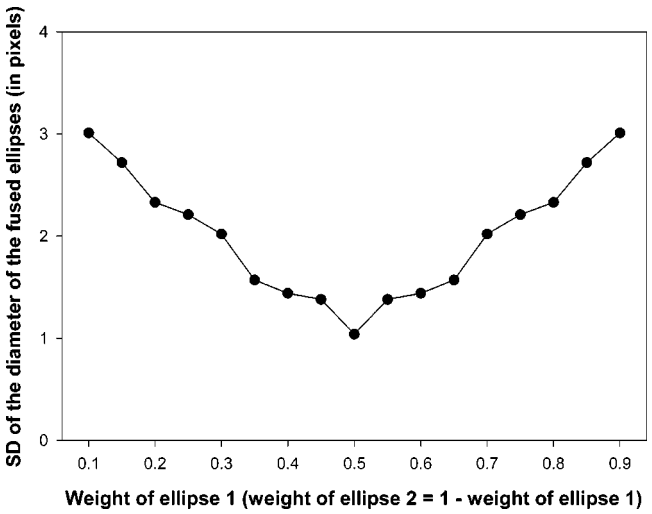

FIG. 10. Standard deviation of the diameters of the fused ellipses. The diameters were calculated from the distance of each point of the contour to the center.

IV. DISCUSSION

The fast development of vascular medical imaging devices leads to an increase of useful data about vascular disease. Accurate images of lumen contours are made available, providing reliable estimation of vessel morphology. However, the existing modalities differ to a great extent in terms of physical properties involved in the image acquisition processes and, consequently, the images obtained have to be analyzed carefully by taking into account the relative limits and performance of the chosen modalities. Furthermore and mainly for cost and time reasons, physicians have to make a choice between accessible devices during their clinical activities. In this framework of multimodality image acquisition, the aim of the work was to use a phantom to compare vascular images and to emphasize the geometric accuracy of the most common modalities used in radiology. The use of a vascular phantom[9] was easily justified by the fact that it is almost the only way to obtain and assess consistent quantitative data on the accuracy of a technique. Furthermore, it ensures the reproducibility of the image combination method that was presented, since all images were acquired from the same phantom. The fiducial markers at well-known positions inside the phantom permitted us to calibrate the images and also to have reliable points assisting the spatial registration. Finally, the known dimensions of the vessel segments (known by construction and verified *a posteriori* on histological slices) leaded to a precise comparison of geometric measurements and underlined disparities inherent to each modality. It is, however, important to notice that the situation in this phantom study was ideal: slices were perpendicular to the vessels which facilitated the measurement of the diameters. Of course in a real situation this is nearly impossible to perform, except in long and straight arteries. It would be of great interest to design and study curvilinear and realistic vessels in future developments.

It was chosen to use the maximum of the gradient norm to segment the limit between the lumen and inner wall of the vessel parts. A number of other methods could have been applied, but the latter has the interest to not depend on a threshold.

In the modeling part of the fusion, it may be emphasized that the imprecision or variability that may have been induced by any presegmentation method was taken into account by building fuzzy contours. The advantage of fuzzy set techniques in image processing and image segmentation relies on the fact that they are able to represent ill-defined clusters or classes in a natural approach by assigning continuous levels of membership to a given set.[26] The imprecision related to these ill-defined descriptions is depicted as degrees of belonging, typicality, or compatibility. A consequence of the theory is that the membership degree of a voxel to a fuzzy contour does not depend on its membership

to the lumen or to the vessel. This point is retrieved when one expresses fuzzy sets as possibility distributions: an event (e.g., ''a voxel v belonging to the contour'') and the corresponding complementary event (''v belonging to the tissue or to the lumen'') may have possibilities equal to 1. This latter property makes possibilistic and probabilistic approaches very different. However, the actual property that really makes the popularity of possibilistic methods is the ability to manage and quantify uncertainty thanks to powerful fusion operators. The behavior of such operators can be chosen according to specific requirements, for example, the degree of discordance between images. A t-norm with a severe conjunctive behavior was chosen in this study. When fusing two images, this operator does prefer the one that provides the smallest possibility or fuzzy contour membership degree, leading to a decrease of imprecision because the area of the fused fuzzy contour becomes smaller than the area of both initial fuzzy maps. This point can also be seen as a decrease of fuzziness.

The construction of fuzzy contours was realized with a classical linear membership function,[21] characterized by two thresholds. A simulation on generated test images was performed to prove the robustness of the fusion process with respect to these thresholds. A set of values (low threshold $=0.025$ and high threshold$=0.175$) gave very good results during the simulation and they were chosen to fuse the phantom multimodality vascular images for this reason.

According to the results of the present study, XCT is the most accurate and robust technique when one wants to measure the inner diameter of a vessel, and for a wide range of vessel sizes, down to values below 1 mm, approximately. This result is in accordance with conclusions found by others.[8] IVUS gave the best results in our study but the finite size of the endovascular catheter is a limitation: very small diameters could not be evaluated because the probe cannot be introduced into the lumen. This was the case in our experiments. On the other hand, IVUS can depict the nature of the vascular wall and tissue. Here again, the choice of a particular imaging technique is governed by clinical interest and procedure involved. For technical reasons, only three B-mode US scans could be analyzed. The 3D scan of the smallest 0.93-mm-diameter segment could not be processed because the lumen was not detectable, maybe because of the limited spatial resolution of the instrument. The accuracy of B-mode obtained in this study was comparable to the literature. For instance an error between 2% and 3% was found in Beux *et al.*[7] Finally, x-ray digital subtraction angiography tended to underestimate the diameters, which potentially corresponded to a deficient calibration, performed manually with a caliper. In spite of careful calibration using fiducial marker locations, an important underestimation error was observed for each vessel segment (see Table I). A lower accuracy of uniplanar and biplanar angiography compared to IVUS also was reported by Cooper *et al.*[6] However, a better spatial resolution could have been obtained by using a three-dimensional digital substraction angiography unit equipped with a 1024 matrix image intensifier (peripheral or neuroangiography unit) instead of a 512 matrix image intensifier (cardiology unit).[27] This last modality was not tested in this study and it would probably lead to good geometrical accuracy.

A noticeable remark concerning the fused images is the decrease of variability when measuring diameters, compared to single modalities. This point could be explained by the fact that, first, the fusion operator followed by the defuzzyfication acts like an average procedure and second, they reduce the local variations by smoothing the contours. The fusion process also showed better robustness with respect to the different diameters than single modalities alone, as shown by the MRE values obtained. Unexpectedly, the XCT-B-mode US fusion resulted in a better accuracy than XCT or B-mode alone. This surprising statement can be attributed to the fact that the mean diameter of the fused images, for the 4.16 and 2.34 mm vessels, was lower than the mean diameter of the XCT and US images (see Table I). This point could be explained by the noisy content of the US images that was erased by fusion with the high weighted XCT images used here. A last comment may be added in favor of the weighting operator used to manage the reliability of the fusion process. In the current study, the weights for XCT, IVUS, MRI, and B-mode US were 1, 0.95, 0.8, and 0.7, respectively. This was selected by taking into account the geometrical accuracy of each modality, as known from the literature. In a clinical context, it may be advantageous to provide flexibility in the values of those weights. For example, according to the quality of a given exam and the type of vascular pathology investigated, it would be of interest to change the weights in accordance to the clinician's ''confidence'' in the images to be fused. Although this was not the scope of the present study, this possibility may be envisaged if one considers the development of a commercial software for clinical use or for the assessment of new imaging technologies.

V. CONCLUSION

When estimating lumen vessel diameters, XCT provided the most precise data for a wide range of vessel widths, while MRI significantly overestimated the smallest diameters (<3 mm). IVUS images at 20 MHz also gave the best results except for small vessels that could not be investigated because of the finite catheter size. B-mode US at 6 MHz was unable to image the vessel below 1 mm diameter, but the largest ones were estimated within acceptable limits. Finally the results showed that, in spite of their high spatial resolution, DSA measurements must be interpreted carefully because of the calibration step that may hamper the accuracy.

The second part of the work dealt with image fusion, an image processing step justified by the increasing amount of data available in medical imagery. The assessment of the fusion method is encouraging since first, it leads to a precise segmentation of the lumen by reducing relative errors compared to the gold standard, and second, it allows the variability of diameter values to be decreased.

To conclude, this work emphasized the utility of the designed multimodal vascular phantom as a validation tool. Further investigations will study abnormal vessels with real-

istic 3D geometries, with and without stents. Such vessels can be modeled within the phantom.

ACKNOWLEDGMENTS

The authors acknowledge Dr. Robert Boileau for his helpful contribution in the statistical data analysis (Table II), and Dr. Louis-Gilles Durand from the Laboratory of Biomedical Engineering of the Clinical Research Institute of Montreal for providing the motor assembly used to produce the 3D B-mode ultrasound images by linear translation of the ultrasound probe. This work was supported by grants from the Canadian Institute of Health Research (G.C., G.S., No. MOP-53244) and Valorisation-Recherche Québec (group Grant No. 2200-094), and by research scholarship awards from the Fonds de la Recherche en Santé du Québec (G.C. and G.S.).

[a]Send correspondence to Dr. Guy Cloutier, Director, Laboratory of Biorheology and Medical Ultrasonics, Research Center, Centre Hospitalier de l'Université de Montréal, 2099 Alexandre de Sève (room y-1619), Montréal, Québec H2L 2W5, Canada. Electronic mail: guy.cloutier@umontreal.ca

[1] P. M. White, E. Teadsale, J. M. Wardlaw, and V. Easton, "What is the most sensitive non-invasive imaging strategy for the diagnosis of intracranial aneurysms?," J. Neurol., Neurosurg. Psychiatry **71**, 322–328 (2001).

[2] E. I. Bluth, J. H. Sunshine, J. B. Lyons, C. A. Beam, L. A. Troxclair, L. Althans-Kopecky, P. E. Crewson, M. A. Sullivan, D. H. Smetherman, P. A. Heidenreich, H. L. Nieman, and J. H. Burkhardt, "Power Doppler imaging: initial evaluation as a screening examination for carotid artery stenosis," Radiology **215**, 791–800 (2000).

[3] C. S. van Rijswijk, E. van der Linden, H. J. van der Woude, J. M. van Baalen, and J. L. Bloem, "Value of dynamic contrast-enhanced MR imaging in diagnosing and classifying peripheral vascular malformations," Am. J. Roentgenol. **178**, 1181–1187 (2002).

[4] G. G. Hartnell, "Imaging of aortic aneurysms and dissection: CT and MRI," J. Thorac. Imaging **16**, 35–46 (2001).

[5] R. Vosshenrich, B. Engeroff, C. Muller, U. Fischer, and E. Grabbe, "Experimental evaluation of vessel diameter from 0.3 to 8 mm in CE MR angiography," Rofo Fortschr Geb Rontgenstr Neuen Bildgeb Verfahr **173**, 842–847 (2001).

[6] B. Z. Cooper, J. D. Kirwin, T. F. Panetta, F. M. Weinreb, J. A. Ramirez, J. G. Najjar, S. B. Blattman, W. Rodino, and M. Song, "Accuracy of intravascular ultrasound for diameter measurement of phantom arteries," J. Surg. Res. **100**, 99–105 (2001).

[7] F. Beux, S. Carmassi, M. V. Salvetti, L. Ghiadoni, Y. Huang, S. Taddei, and A. Salvetti, "Automatic evaluation of arterial diameter variation from vascular echographic images," Ultrasound Med. Biol. **27**, 1621–1629 (2001).

[8] J. Bushberg, J. Anthony Seibert, E. Leidholt, and J. Boone, *The Essential Physics of Medical Imaging*, 2nd ed. (Lippincott Williams & Wilkins, Philadelphia, 2002).

[9] G. Cloutier, G. Soulez, S. D. Qanadli, P. Teppaz, L. Allard, Z. Qin, F. Cloutier, and L. G. Durand, "A multimodality vascular imaging phantom with fiducial markers visible in DSA, CTA, MRA and ultrasound," Med. Phys. **31**, 1424–1433 (2004).

[10] N. Boussion, L. Cinotti, V. Barra, P. Ryvlin, and F. Mauguière, "Extraction of epileptogenic foci from PET and SPECT images by fuzzy modeling and data fusion," Neuroimage **19**, 645–654 (2003).

[11] F. Azuaje, W. Dubitzky, N. Black, and K. Adamson, "Improving clinical decision support through case-based data fusion," IEEE Trans. Biomed. Eng. **46**, 1181–1185 (1999).

[12] B. Solaiman, R. Debon, F. Pipelier, J. M. Cauvin, and C. Roux, "Information fusion: application to data and model fusion for ultrasound image segmentation," IEEE Trans. Biomed. Eng. **46**, 1171–1175 (1999).

[13] F. Maes, A. Collignon, D. Vandermeulen, G. Marchal, and P. Suetens, "Multimodality image registration by maximization of mutual information," IEEE Trans. Med. Imaging **16**, 187–198 (1997).

[14] J. Hajnal, D. Hill, and D. Hawkes, *Medical Image Registration* (CRC, Boca Raton, 2001).

[15] S. Glantz, *Primer of Biostatistics*, 4th ed. (McGraw-Hill, New York, 1997).

[16] L. Zadeh, "Fuzzy sets," Inf. Control **8**, 338–353 (1965).

[17] G. Borgefors, "Distance transformations in arbitrary dimensions," Comput. Vis. Graph. Image Process. **27**, 321–345 (1985).

[18] L. Zadeh, "Fuzzy sets as a basis for a theory of possibility," Fuzzy Sets Syst. **1**, 3–28 (1978).

[19] I. Bloch, "Information combination operators for data fusion: a comparative review with classification," IEEE Trans. Syst. Man Cybern. **26**, 52–67 (1996).

[20] D. Dubois and H. Prade, "Combination of fuzzy information in the framework of possibility theory," in *Data Fusion in Robotics and Machine Intelligence*, edited by M. A. Abidi and R. C. Gonzalez (Academic, San Diego, 1992), pp. 481–505.

[21] B. Bouchon-Meunier, "Uncertainty management in medical applications," in *Nonlinear Biomedical Signal Processing, Volume 1*, edited by M. Akay (IEEE Press series on Biomedical Engineering, Series editors, New York, 2000), pp. 1–26.

[22] H. I. Manninen, R. L. Vanninen, M. Laitinen, H. Rasanen, P. Vainio, J. S. Luoma, T. Pakkanen, H. Tulla, and S. Yla-Herttuala, "Intravascular ultrasound and magnetic resonance imaging in the assessment of atherosclerotic lesions in rabbit aorta. Correlation to histopathologic findings," Invest. Radiol. **33**, 464–471 (1998).

[23] G. Cron and B. Dubuisson, "A weighted fuzzy aggregation method," *Fuzz-IEEE 98 Anchorage* (1998), pp. 675–680.

[24] J. Serra, *Image Analysis and Mathematical Morphology* (Academic, London, England, 1982).

[25] I. Bloch and H. Maître, "Fuzzy mathematical morphologies: a comparative study," Pattern Recogn. **9**, 1341–1387 (1995).

[26] V. Barra and J. Y. Boire, "Automatic segmentation of subcortical brain structures in MR images using information fusion," IEEE Trans. Med. Imaging **20**, 549–558 (2001).

[27] K. Bendib, C. Poirier, P. Croisille, J. Roux, D. Revel, and M. Amiel, "Characterization of arterial stenosis using 3D imaging. Comparison of 3 imaging techniques (MRI, spiral CT and 3D DSA) and 4 display methods (MIP, SR, MPVR, VA) by using physical phantoms," J. Radiol. **80**, 1561–1567 (1999).